

# Lens Models with Density Cusps

N.W. Evans and M. Wilkinson

*Theoretical Physics, Department of Physics, 1 Keble Road, Oxford, OX1 3NP*

## ABSTRACT

Lens models appropriate for representing cusped galaxies and clusters are developed. The analogue of the odd number theorem for cusped density distributions is given. Density cusps are classified into strong, isothermal or weak, according to their lensing properties. Strong cusps cause multiple imaging for any source position, whereas isothermal and weak cusps give rise to only one image for distant sources. Isothermal cusps always possess a pseudo-caustic. When the source crosses the pseudo-caustic, the number of images changes by unity.

Two families of cusped galaxy and cluster models are examined in detail. The double power-law family has an inner cusp, followed by a transition region and an outer envelope. *One member of this family – the isothermal double power-law model – possesses an exceedingly scarce property, namely, the lens equation is exactly solvable for any source position.* This means that the magnifications, the time delay and the lensing cross-sections are all readily available. The model has a three dimensional density that is cusped like  $r^{-2}$  at small radii and falls off like  $r^{-4}$  asymptotically. Thus, it provides a very useful representation of the lensing properties of a galaxy or cluster of finite total mass with a flat rotation curve. The second set of models studied is the single power-law family. These are single density cusps of infinite extent. The properties of the critical curves and caustics and the behaviour of the lenses in the presence of external shear are all discussed in some detail.

**Key words:** gravitational lensing – galaxies: structure

## 1 INTRODUCTION

The aim of this paper is to examine the properties of lens models with density cusps. High-resolution imaging of the the nuclei of early-type galaxies by the Hubble Space Telescope (e.g., Lauer et al. 1995) have provided abundant examples of cusps. In almost all early-type galaxies, the logarithmic gradient of the surface brightness with respect to projected radius is constant right down to the very centre. Galaxy cores are hardly ever observed. This observational evidence for the ubiquity of central cusps is reinforced by theoretical suggestions of dynamical processes by which cusps can grow in the basins of potential wells (e.g., Bahcall & Wolf 1976; Faber et al. 1996; Evans & Collett 1997). Further, the influential numerical simulations by Navarro, Frenk & White (1996) of galaxy formation in hierachical clustering cosmogonies found striking evidence for a universal cusped density law for dark matter haloes and clusters.

This change in our understanding of the structure of galaxies and clusters motivates our study of geometrically thin, centrally cusped gravitational lenses. Hitherto, the emphasis in gravitational lensing studies has largely been placed on non-singular models, such as softened isothermal spheres and ellipsoids or Plummer models (e.g., Blandford & Kochanek 1987; Kochanek 1996; Keeton & Kochanek 1997; Schneider, Ehlers & Falco 1992, chap. 8). For such non-singular lenses, it is well-known that the total number of

images is odd and that the number of even parity images exceeds the number of odd parity images by one (e.g., MacKenzie 1985; Burke 1981; Schneider, Ehlers & Falco 1992, chap. 5). This paper begins with an outline of general results on geometrically thin, centrally cusped lens models appropriate for galaxies and clusters. In Section 3, a new and simple family of axisymmetric cusped lenses, the double power-law lenses, is presented, together with an application to radial arcs in clusters. Section 4 studies one member of this family, the isothermal double-power lens, in detail. It is worthy of special scrutiny, as the lens equation is solvable for any source position. This property is possessed by only two other known circularly symmetric lenses (the Schwarzschild lens and the isothermal sphere). Section 5 examines a family of density cusps of infinite extent, with equipotentials that are similar concentric ellipses. The isothermal model in this family has already been extensively investigated (e.g., Kassiola & Kovner 1993). The remaining members have not been examined in detail as isolated lenses, although the statistical properties of ensembles of these models have been studied in two classic papers (Blandford & Kochanek 1987; Kochanek & Blandford 1987).

In all of the following sections, we use the notation and conventions of the admirable text-book of Schneider, Ehlers & Falco (1992). In particular, we use  $(x_1, x_2)$  as Cartesian coordinates in the lens plane and  $(y_1, y_2)$  as Cartesian coordinates in the source plane. The Poisson equation relating

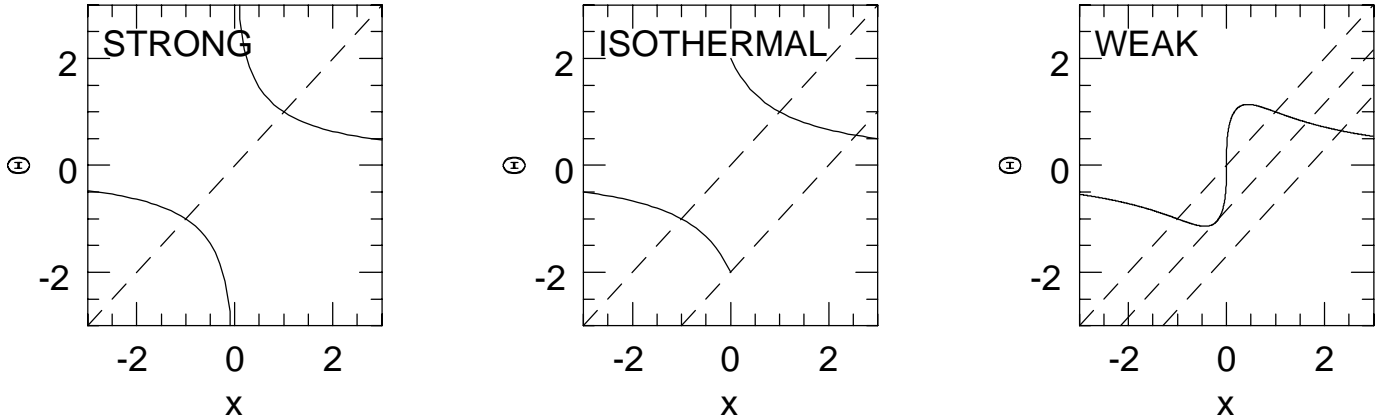


**Figure 1.** Multiple image diagrams for strong, isothermal and weak cusps. Typical  $x - y$  curves are shown in dashed lines for a number of source positions. Multiple imaging takes place for the source position  $y_1$  if the line  $x - y_1$  intersects the deflection angle curve more than once. In the strong cusp, no matter how distant the source position, the observer sees at least two images. In the isothermal cusp, multiple imaging only takes place if the source is sufficiently close to the cusp. For sources far enough away, only one image is observed. In the weak cusp, three images are seen for source close to the cusp, one image for distant sources. The change-over in the number of images occurs as the source crosses the radial caustic, as shown.

the convergence  $\kappa$  and the deflection potential  $\psi$  is scaled to read  $\nabla^2\psi = 2\kappa$ . The deflection angle  $\Theta$  is just  $\nabla\psi$ .

## 2 GENERAL THEOREMS

To orient ourselves, we start with the simpler case of axisymmetric lenses with density cusps. Theorems for general cusped lenses are deduced in Section 2.2.

### 2.1 Axisymmetric Lenses

Let us consider a geometrically thin, axisymmetric lens with convergence  $\kappa(R)$ , where  $R = |\underline{x}|$ . For an axisymmetric lens, the ray trace equation is one-dimensional, as all light rays emanating from the source and received by the observer lie in the common plane incorporating the observer, lens and source. Let us choose coordinates in the lens plane so that  $\underline{x} = (x, 0)$  and in the source plane so that  $\underline{y} = (y, 0)$ . The surface density is assumed to be piecewise continuous everywhere except at the central cusp  $R = 0$ . We suppose that the deflection angle vanishes asymptotically, or, equivalently, the convergence falls off at large radii faster than  $1/R$ , i.e.,

$$\lim_{R \rightarrow \infty} R\kappa(R) = 0. \quad (2.1)$$

Let the convergence diverge at the origin like

$$\lim_{R \rightarrow 0} \kappa(R) = O(R^{-\gamma}). \quad (2.2)$$

Then:

(1) If  $1 < \gamma < 2$ , multiple imaging occurs for any position of the source  $y$ , no matter how large. The model is said to

have a strong cusp.

(2) If  $\gamma = 1$ , the cusp is isothermal. Multiple imaging occurs for some source positions. For sufficiently large values of  $y$ , there is only one image. For sufficiently small values of  $y$ , there are at least two images.

(3) If  $0 < \gamma < 1$ , multiple imaging occurs for some source positions. For sufficiently large values of  $y$ , there is only one image. For sufficiently small values of  $y$ , there are at least three images. The model is said to have a weak cusp.

(4) If  $\gamma \leq 0$ , the model is uncusped in projection. A necessary and sufficient condition for multiple imaging is that the central convergence  $\kappa(0)$  must exceed unity (Schneider, Ehlers & Falco 1992, p. 236). We remark that models which are uncusped in projection may still possess a mild cusp in the three-dimensional luminosity density.

These statements are readily proved. As the cusp is approached, the deflection angle  $\Theta = \nabla\psi$  behaves like

$$\lim_{R \rightarrow 0} \Theta = O(R^{-\gamma+1}). \quad (2.3)$$

Near the cusp, the deflection angle vanishes if  $\gamma < 1$ , tends to a constant value if  $\gamma = 1$  and diverges if  $\gamma > 1$ . Now, the deflection angle is an odd function of  $x$ . So, this implies that  $\Theta$  is discontinuous at  $x = 0$  for isothermal cusps, while  $\Theta$  possesses a singularity at  $x = 0$  for strong cusps. The gradient of the deflection angle behaves like

$$\lim_{R \rightarrow 0} \frac{d\Theta}{dR} = O(R^{-\gamma}). \quad (2.4)$$

This diverges for all cusped models.

Figure 1 shows multiple image diagrams for strong, isothermal and weak cusps in typical centrally condensed galaxy or cluster models. The graphs show the deflection

angle  $\Theta$ , together with  $x - y$  lines for a number of values of the source position. The location of the images is given by the solutions of the lens equation, and therefore by the intersection of the  $x - y$  lines with the deflection angle. So, for strong cusps, it is evident from Fig. 1 that there are always two images, irrespective of the distance of the source. Isothermal cusps have the curious property that the number of images can change by one, as the source position is moved outward across a curve that we shall call *the pseudo-caustic*. This is illustrated in the second panel of Fig. 1. This curiosity has previously been noticed in analyses of the singular isothermal sphere and ellipsoid (Kovner 1987a; Kormann, Schneider & Bartelmann 1994; Schneider, Ehlers & Falco 1992, p. 243). Weak cusps always exhibit multiple imaging for sufficiently small  $y$ . As the source is moved away, there comes a critical point when it crosses the radial caustic and the number of images diminishes by two. This is shown in the third panel of Fig. 1.

Let us note that the observations of the centres of early-type galaxies indicate that strong, weak and isothermal cusps all can occur. For example, table 2 of Faber et al. (1997) gives the cusp slope  $\gamma$  for a sample of 61 elliptical galaxies. The observationally fitted values of  $\gamma$  lie in the range  $0.0 < \gamma < 1.21$ . NGC 1199 is an example of a galaxy with a strong cusp, while NGC 4467 has an isothermal cusp. Weak cusps are the most predominant in Faber et al.'s (1997) sample. The cosmological simulations of Navarro, Frenk & White (1996) suggest that dark matter haloes possess a universal density law with a logarithmically singular surface density. Subsequently, numerical investigations (Fukushige & Makino 1997; Moore, Governato, Quinn, Stadel & Lake 1997) together with theoretical arguments (Evans & Collett 1997) indicated that the original work had underestimated the severity of the cusp. The weight of the evidence now suggests that dark haloes have three-dimensional density cusps like  $\rho \sim r^{-4/3}$ . In projection, this becomes  $\kappa \sim r^{-2/3}$  and so lies within the weak cusp régime.

## 2.2 General Lenses and Index Theorems

There is a general theorem for non-singular lenses that states that the total number of images is odd and that the number of even parity images exceeds the number of odd parity images by one (MacKenzie 1985; Burke 1981; Fukuyama & Okamura 1997). The image type is classified by studying the Jacobian matrix of the Fermat potential  $\phi$ . If both the eigenvalues are positive or both are negative, then the images are of type I and III respectively. Such images have even parity and correspond to minima or maxima of the Fermat potential. If one of the eigenvalues is positive and one negative, the image is of type II. Such images have odd parity and correspond to saddle-points of the Fermat potential. The odd number theorem is usually stated in the form

$$n_I - n_{II} + n_{III} = 1, \quad (2.5)$$

where  $n_I$  is the number of images of type I and so on. It follows from this that the total number of images ( $n_I + n_{II} + n_{III}$ ) is necessarily odd.

To set the notation, let us quickly re-derive the odd number theorem for non-singular lenses. Introducing  $z = x_1 + ix_2$ ,  $\bar{z} = x_1 - ix_2$ , then the lens equation becomes just

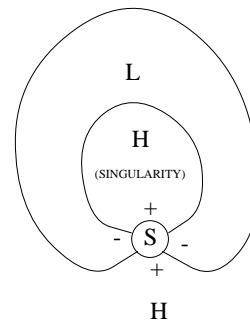


**Figure 2.** The only possible two image topography (the limaçon) of the Fermat surface for lenses with strong density cusps. The saddle point is marked by S and the + and - signs indicate regions where the Fermat surface is higher (H) and lower (L) than the saddle. An image of type II occurs at the saddle, an image of type I at the minimum. The density singularity is marked.

(e.g., Witt 1990)

$$\frac{\partial \phi}{\partial \bar{z}} = \phi_{\bar{z}} = 0. \quad (2.6)$$

Let  $C_z$  be a contour enclosing some point P in the complex  $z$  plane. The index of the map  $\omega = \phi_{\bar{z}}(z)$  at P is

$$\text{Ind}(\phi_{\bar{z}}, P) = \frac{1}{2\pi i} \oint_{C_\omega} d \ln \omega, \quad (2.7)$$

where  $C_\omega$  is the image of  $C_z$ . So, the index is the number of times the image of P in the complex  $\omega$ -plane is encircled, as P in the complex  $z$ -plane is encircled once in the anti-clockwise direction. If  $C_z$  does not enclose any zeroes or singular points, the index vanishes. It is straightforward to show (e.g., Schneider, Ehlers & Falco 1992, p. 174) that the index of an extremum of the Fermat potential is +1, whereas the index of a saddle point is -1. Provided the deflection angle tends to zero at large radii, then it must be true asymptotically that

$$\phi_{\bar{z}} = \frac{1}{2}|z - z_s| + o(|z|), \quad (2.8)$$

where  $z_s = y_1 + iy_2$  is the complex position of the source. So, the point at infinity is a pole and it has an index of unity. By shrinking the contour so that it becomes enmeshed with the singular points and zeroes, it follows that the sum of all the indices must be equal to unity. If the lens is non-singular, there are no poles and only the contributions of the zeroes must be taken into account, i.e.,

$$1 = \text{Ind}(\phi_{\bar{z}}, \infty) = \sum_i \text{Ind}(\phi_{\bar{z}}, P_i) = n_I - n_{II} + n_{III}. \quad (2.9)$$

This is the odd number theorem and holds good only for non-singular lenses with convergence falling off faster than  $1/|z|$  at large radii.

What is the analogue of this theorem for general lenses with density cusps? A careful examination of the density singularity at the origin of the  $z$ -plane is required to establish its index. Near the origin, the lens equation can always be cast into the form

$$\phi_{\bar{z}} = \frac{1}{2}|z - z_s| + \frac{Az^{1-\gamma/2}}{\bar{z}^{\gamma/2}}, \quad (2.10)$$

where  $A$  is a constant (for circular lenses) or a real function of the phase (for non-axisymmetric lenses) and the

**Table 1.** Some simple potentials corresponding to the convergence of the double power-law family as given in eqs. (3.3) and (3.8). (Below,  $\ell$  and  $n$  are natural numbers. The summands are empty if  $\ell = 0$  or  $n = 0$ .)

---

$L = 1$	$N = 2n$	$\psi(R) = \frac{8C\alpha^2}{2n+1} \left[ \log(1 + \sqrt{R^{1/\alpha} + 1}) - \sum_{k=1}^n \frac{1}{2k-1} \frac{1}{(1 + R^{1/\alpha})^{k-1/2}} \right]$
$L = 1$	$N = 2n + 1$	$\psi(R) = \frac{2C\alpha^2}{n+1} \left[ \log(1 + R^{1/\alpha}) - \sum_{k=1}^n \frac{1}{k} \frac{1}{(1 + R^{1/\alpha})^k} \right]$
$L = 2\ell$	$N = 1$	$\psi(R) = \frac{8C\alpha^2}{2\ell+1} \left[ \log(R^{1/(2\alpha)} + \sqrt{R^{1/\alpha} + 1}) - \sum_{k=1}^{\ell} \frac{1}{2k-1} \left( \frac{R^{1/\alpha}}{1 + R^{1/\alpha}} \right)^{k-1/2} \right]$
$L = 2\ell + 1$	$N = 1$	$\psi(R) = \frac{2C\alpha^2}{\ell+1} \left[ \log(1 + R^{1/\alpha}) - \sum_{k=1}^{\ell} \frac{1}{k} \left( \frac{R^{1/\alpha}}{1 + R^{1/\alpha}} \right)^k \right]$

---

sub-dominant terms have been neglected. Substituting  $z = \epsilon \exp(i\theta)$ , this becomes

$$\phi_{\bar{z}} = \frac{1}{2} |\epsilon \exp(i\theta) - z_s| + A \epsilon^{1-\gamma} \exp(i\theta). \quad (2.11)$$

Letting  $\epsilon \rightarrow 0$  so that the contour is wrapped tightly around the origin, we deduce that the first term is dominant in the case of weak cusps ( $0 < \gamma < 1$ ) and the second term is dominant in the case of strong cusps ( $1 < \gamma < 2$ ). In the limit, the vector field  $\phi_{\bar{z}}$  is constant for weak cusps, so the the index of the origin is 0 and the odd number theorem (2.5) still holds good. For strong cusps, a different situation obtains. The index of the origin is +1, as the vector field is radial in the limit  $\epsilon \rightarrow 0$ . Lens models with strong cusps have an even number of images, as

$$n_{\text{I}} - n_{\text{II}} + n_{\text{III}} = 0. \quad (2.12)$$

The number of even parity images is equal to the number of odd parity images.

The instance of isothermal cusps ( $\gamma = 1$ ) is more subtle. Now both terms in (2.10) matter and the index of the origin depends on the position of the source  $z_s$ . As  $\epsilon \rightarrow 0$ , the lens equation (2.11) becomes

$$\phi_{\bar{z}} = \frac{1}{2} |z_s| + A \exp(i\theta), \quad (2.13)$$

where  $A = \psi_{\bar{z}}$  which depends only on the phase for models with isothermal cusps. If  $|z_s| < 2|\psi_{\bar{z}}|$ , then the index of the origin is +1, otherwise the index of the origin is 0. This equation therefore defines a curve in the source plane – the pseudo-caustic. If the source is outside the pseudo-caustic, there is an odd number of images according to (2.5). Crossing the pseudo-caustic produces an additional, single image of type II initially at the origin. Once the source is within the pseudo-caustic, there is an even number of images according to (2.12). Note that the pseudo-caustic differs from a true caustic because the magnification of a point source is finite (not infinite) and because the number of images changes by one (not two). The analogues in the lens plane are the pseudo-critical curves.

As is well-known (Blandford & Narayan 1986; Schneider, Ehlers & Falco 1992, p. 178), the topography of the Fermat surface for non-singular lenses can be classified in terms of the local structure at saddle points. For three image geometries, the shape of the critical isochrone corresponds either to a lemniscate or a limaçon. For five image geometries,

there are six possible topographies given by joining lemniscates and limaçons. These theorems still hold for lenses with weak density cusps. But, if the lens possesses a strong density cusp, then the topography of the Fermat surface is more restricted. For two image geometries, the only possibility is the limaçon illustrated in Fig. 2. One of the images occurs at the saddle point marked by S, one in the basin of the Fermat surface. The density cusp corresponds to the highest point. For four image geometries, there are five possible topographies, given by joining at least one limaçon to either a lemniscate or a limaçon.

### 3 THE DOUBLE POWER-LAW LENSES

We now present a new family of axisymmetric lenses with central density cusps, the double power-law lenses. Section 3.1 explains our strategy for locating the models with simple potential-convergence pairs. The following sections examine properties and applications of the models in detail.

#### 3.1 The Potential-Convergence Pair

Let us consider the family of cusped lenses with surface density  $\Sigma$  as a function of projected radius  $\xi$  given by

$$\Sigma(\xi) = \frac{C \xi_c^\beta}{\xi^\gamma (\xi^{1/\alpha} + \xi_c^{1/\alpha})^{\alpha(\beta-\gamma)}}. \quad (3.1)$$

Here,  $(\alpha, \beta, \gamma)$  are positive constants and  $\xi_c$  is a scale-length. By choosing the scale in the lens plane as  $\xi_c$ , then the convergence  $\kappa$  is defined as (e.g., Schneider, Ehlers & Falco 1992, chap. 5)

$$\kappa(R) = \frac{\Sigma(R\xi_c)}{\Sigma_{\text{crit}}}, \quad \Sigma_{\text{crit}} = \frac{c^2 D_s}{4\pi G D_d D_{ds}}, \quad (3.2)$$

where  $\Sigma_{\text{crit}}$  is the critical surface density and  $D_s, D_d$  and  $D_{ds}$  are the observer-source, the observer-lens and the lens-source distances respectively. For our model (3.1), this gives

$$\kappa(R) = \frac{C}{R^\gamma (R^{1/\alpha} + 1)^{\alpha(\beta-\gamma)}}. \quad (3.3)$$

At small radii, the convergence is cusped like  $R^{-\gamma}$ , whereas in the outer parts, it falls like  $R^{-\beta}$ . The parameter  $\alpha$  controls the extent of the transition region between the cusp

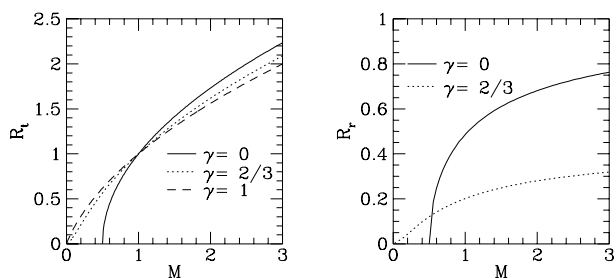


**Figure 3.** The variation of the radii of the tangential and radial critical circles with total projected mass for various values of  $\gamma$ . Note that radial critical curves and caustics do not exist if  $\gamma \geq 1$ , as is evident on referring back to the multiple imaging diagrams of Fig. 1.

and the envelope. The lens models (3.3) are clearly inspired by the ‘Nuker’ profile introduced by Gebhardt et al. (1997) and Faber et al. (1997). These authors show that it provides a compact description of the surface brightness of early-type galaxies. The lens models (3.3) are also related to the three-dimensional elliptical galaxy models introduced by Hernquist (1990) and studied by Zhao (1996). The normalisation constant  $C$  is related to the total mass  $\mathcal{M}$  by

$$\mathcal{M} = 2C\pi\xi_c^2\Sigma_{\text{crit}}\alpha B(\alpha[2-\gamma], \alpha[\beta-2]), \quad (3.4)$$

where  $B(x, y) = \Gamma(x)\Gamma(y)/\Gamma(x+y)$  is the complete Beta function. For convenience, we also define a dimensionless mass  $M$  such that

$$M = \frac{\mathcal{M}}{2\pi\xi_c^2\Sigma_{\text{crit}}}. \quad (3.5)$$

For the total mass to converge, we must insist that  $\beta > 2$  and that  $\gamma < 2$ .

The solution of the two-dimensional Poisson equation is familiar from the theory of the Newtonian potential of circular cylinders as (e.g., Routh 1892; Ramsey 1940)

$$\psi(R) = 2\log R \int_0^R dr r\kappa(r) + 2 \int_R^\infty dr r\kappa(r) \log r. \quad (3.6)$$

Of course, the first term is the potential of the circular cylinders interior to  $R$ , which attract as if their mass were concentrated on axis. The second term is the potential of the circular cylinders exterior to  $R$ . Integrating (3.6) by parts, we obtain:

$$\psi(R) = 2\log R \int_0^\infty dr r\kappa(r) + 2 \int_R^\infty \frac{dr}{r} \int_r^\infty dr' r' \kappa(r'). \quad (3.7)$$

Substituting the convergence (3.3), we see that in general the potential is not elementary. Of course, there is an enormous advantage to working with models with at least simple deflection angles and preferably simple potentials. So, let us first outline conditions under which these quantities are reducible to a finite number of elementary functions. It is helpful to introduce two constants  $L$  and  $N$  such that

$$L = 2\alpha[2-\gamma] - 1, \quad N = 2\alpha[\beta-2] - 1. \quad (3.8)$$

Making the substitution  $R = \tan^{2\alpha} \theta$ , then the deflection angle is

$$\begin{aligned} \Theta &= \frac{d\psi}{dR} = \frac{4C\alpha}{R} \int_0^\theta d\theta' \sin^L \theta' \cos^N \theta' \\ &= \frac{2C\alpha}{R} B(L/2 + 1/2, N/2 + 1/2; \sin^2 \theta). \end{aligned} \quad (3.9)$$

Here,  $B(x, y; z)$  is the incomplete Beta function (see e.g., Abramowitz & Stegun 1965; Gradshteyn & Ryzik 1980). Amongst other instances, it reduces to a finite number of elementary functions if either (1)  $L$  is an odd natural number and  $N$  is arbitrary, or vice versa, or (2)  $L$  is an even natural number (or zero) and  $N$  is any natural number (or zero), or vice versa.

The potential can similarly be reduced to

$$\begin{aligned} \psi &= 4C\alpha \log R \int_0^{\pi/2} d\theta' \sin^L \theta' \cos^N \theta' \\ &+ 8C\alpha^2 \int_\theta^{\pi/2} \frac{d\theta'}{\sin \theta' \cos \theta'} \int_{\theta'}^{\pi/2} d\phi \sin^L \phi \cos^N \phi. \end{aligned} \quad (3.10)$$

A consultation of the discussion in sections 2.51 and 2.52 of Gradshteyn & Ryzik (1980) reveals that the indefinite integration in (3.10) is elementary if  $L$  and  $N$  are natural numbers (or zero), at least one of which is odd. Let us note explicitly that if  $L$  and  $N$  are both even natural numbers (or zero), the potential is not elementary as it ultimately depends on the transcendent integral (2.644.5) of Gradshteyn & Ryzik (1980).

Some simple examples of lens models with convergence (3.3) possessing elementary potentials are given in Table 1. Henceforth, we specialise to the case  $L = 1, N = 1$  for definiteness.

### 3.2 The $L = 1, N = 1$ Family

Here, the potential-convergence pair is just

$$\kappa = \frac{M(2-\gamma)}{R^\gamma(1+R^{2-\gamma})^2}, \quad \psi = \frac{2M}{2-\gamma} \log(1+R^{2-\gamma}). \quad (3.11)$$

If  $1 < \gamma < 2$ , the lens has a strong cusp. This becomes isothermal when  $\gamma = 1$ . For  $0 < \gamma < 1$ , the lens possesses a weak cusp. The instance  $\gamma = 0$  is the uncusped Plummer model, discussed in detail in Schneider, Ehlers & Falco (1992, chap. 8). Models with  $\gamma < 0$  are unrealistic, as the density is not centrally concentrated.

The scaled deflection angle  $\Theta$  at a displacement  $x$  in the lens plane is

$$\Theta = \nabla\psi = \frac{2M\text{sign}(x)|x|^{1-\gamma}}{1+|x|^{2-\gamma}}, \quad (3.12)$$

where  $|x| = R$ . In the lens plane, the radius of the tangential critical circle  $R_t$  is given by

$$R_t^2(1+R_t^{2-\gamma}) = 2MR_t^{2-\gamma}. \quad (3.13)$$

Generally, this implicit equation cannot be solved analytically. It is exactly solvable when  $\gamma = 1$  to give

$$R_t = \frac{1}{2}\sqrt{1+8M} - \frac{1}{2}, \quad (3.14)$$

when  $\gamma = 0$  to give

$$R_t = \sqrt{2M-1}. \quad (3.15)$$

The tangential critical circles are just the radii of the bright Einstein rings formed when the source is exactly coincident with the lens. The radial critical curves have radius  $R_r$  given by

$$(1 + R_r^{2-\gamma})^2 = 2M((1 - \gamma)R_r^{-\gamma} - R_r^{2-2\gamma}). \quad (3.16)$$

When  $\gamma = 0$ , this is solvable to give

$$R_r^2 = \sqrt{M(4 + M)} - M - 1. \quad (3.17)$$

When  $\gamma \geq 1$ , this equation has no positive root and there is no radial critical curve. As is evident from the multiple imaging diagrams of Fig. 1, isothermal and strong cusps do not have radial critical curves. Figure 3 shows the variation of the critical curves with total projected mass. The curves are labelled with the value of  $\gamma$ . The graph shows that as  $M \rightarrow \infty$ , the tangential critical curves always tend to  $\sqrt{2M}$ , which is the Einstein ring radius of a point mass (let us recall  $M$  is mass measured in units of the  $2\pi\xi_c^2\Sigma_{\text{crit}}$ ).

The tangential caustic coincides with the origin in the source plane  $y_t = 0$ . The radial caustic exists only for weak cusps and is

$$y_r = \frac{R_r(\gamma + 2R_r^{2-\gamma})}{\gamma - 1 + R_r^{2-\gamma}}. \quad (3.18)$$

The radial caustics separates the source domains ( $|y| < y_r$ ) generating three images from those ( $|y| > y_r$ ) generating just one. The magnification is

$$\mu = \left[ 1 - \frac{2MR^{-\gamma}}{1 + R^{2-\gamma}} \right]^{-1} \times \left[ 1 - \frac{2M((1 - \gamma)R^{-\gamma} - R^{2-2\gamma})}{(1 + R^{2-\gamma})^2} \right]^{-1}. \quad (3.19)$$

When  $|y| < y_r$ , the image at  $x > R_t$  is of type I, the image at  $-R_t < x < -R_r$  is of type II and the image at  $-R_r < x < 0$  is of type III. The two components of the shear are

$$\begin{aligned} \gamma_1 &= \frac{M(x_2^2 - x_1^2)(\gamma + 2R^{2-\gamma})}{R^\gamma(1 + R^{2-\gamma})^2}, \\ \gamma_2 &= \frac{-2Mx_1x_2(\gamma + 2R^{2-\gamma})}{R^{2+\gamma}(1 + R^{2-\gamma})^2}. \end{aligned} \quad (3.20)$$

### 3.3 An Application: Radial Arcs

Radial arcs are images of galaxies distorted by foreground clusters. They are elongated in the radial direction, in distinction to the more commonly occurring tangential arcs. Bartelmann (1996) described how, in a situation where both radial and tangential arcs are observed, the positions of the arcs can be used to determine the parameters of the model potential representing the lens. Bartelmann used the three-dimensional density profile suggested by the cosmological simulations of Navarro, Frenk & White (1996), namely:

$$\rho(r) = \frac{\rho_s r_c^3}{r(r_c + r)^2}, \quad (3.21)$$

where  $r$  is the three-dimensional radius and  $\rho_s$  and  $r_c$  are density and length scales. He projected this to obtain the surface density and hence the lens model. He showed that if both the positions and redshifts are available for the tangential and radial arcs, then it is possible to find values for the density and length scales. If the redshifts of the arcs are not

known, it is possible to constrain them. In particular, Bartelmann (1996) pointed out a problem with the density profile (3.21) – for tangential arcs lying within the scale radius, the lens model predicts large values for the radial magnification, which in turn implies that the corresponding sources must be surprisingly thin in the radial direction.

Can the more general family of surface densities (3.1) alleviate the problem described by Bartelmann? In addition to the arbitrary density and length scales (in our notation  $M$  and  $\xi_c$ ), we have the extra parameter  $\gamma$  describing the cusp. By varying the value of  $\gamma$ , can we avoid the problem of large radial magnification at the tangential arcs? Equations (3.13) and (3.16) give the positions of the radial and tangential critical curves for the family of lenses with convergence (3.11). Assuming that the sources producing the radial and tangential arcs are at different redshifts, we rewrite (3.13) and (3.16) as

$$\begin{aligned} R_t^2(1 + R_t^{2-\gamma}) &= 2M_t R_t^{2-\gamma}, \\ (1 + R_r^{2-\gamma})^2 &= 2M_r((1 - \gamma)R_r^{-\gamma} - R_r^{2-2\gamma}), \end{aligned} \quad (3.22)$$

where the subscripts on  $M$  indicate its redshift dependence. Defining the ratio  $\sigma$  by

$$\sigma \equiv \frac{\Sigma_{\text{cr},r}}{\Sigma_{\text{cr},t}} = \frac{M_t}{M_r}, \quad (3.23)$$

we obtain, using (3.22),

$$\sigma(\alpha) = \frac{(1 + R_t^{2-\gamma})(1 - \gamma - R_t^{2-\gamma}\alpha^{2-\gamma})}{\alpha^\gamma(1 + \alpha^{2-\gamma}R_t^{2-\gamma})^2}, \quad (3.24)$$

where  $\alpha = R_r/R_t$ . The value of  $\alpha$  is known from the positions of the radial and tangential arcs. If the redshifts of the arcs are also available, then we can use (3.23) to find the corresponding value of  $\sigma$ . Choosing a value for  $\gamma$ , we can solve (3.24) for  $R_t$ . Since  $R_t = \xi_t/\xi_c$ , and we can observe the value of the physical position of the tangential arc  $\xi_t$ , we can obtain the scale  $\xi_c$ . Finally, (3.22) can be used to obtain the value of the density scale.

Often the redshifts are unavailable and we must proceed more indirectly. As an example, let us consider the lensing cluster MS 2137, which is at a redshift of  $z_c = 0.315$ . In this cluster, a tangential arc has been observed at  $\xi_t = 15''.5$  from the cluster centre. Fort et al. (1992) detected a radial arc in the same cluster at  $\xi_r = 5''.0$  from the cluster centre. To proceed, we assume that  $\xi_c \sim 250h^{-1}$  kpc, a value obtained from numerical simulations of dark matter halos within the CDM cosmogony (cf. Bartelmann 1996). From the observed values of  $\xi_t$  and  $\xi_r$ , we conclude that  $\alpha = 0.32$  and we find that  $R_t \sim 0.2$ . In Fig. 4(a), we have plotted  $\sigma$  as a function of  $\gamma$  for  $R_t = 0.2$  with  $\alpha = 0.32$  (and also for  $0.75\alpha$  and  $1.25\alpha$  to give a feel for the likely uncertainties). By varying the value of  $\gamma$ , we can obtain a wide range in  $\sigma$ . In Fig. 4 (b), we show  $\sigma$  versus the redshift  $z_r$  of the radial arc for a number of different values of the redshift  $z_t$  of the tangential arc. This plot shows that if  $\sigma \lesssim 0.6$ , the redshifts of both sources must be unreasonably large. We should therefore choose a value of  $\gamma$  for which  $\sigma \sim 1$ .

Another constraint on our choice of  $\gamma$  is the radial magnification produced at the position of the tangential arc. Assuming the same value for  $\xi_c$  as before, we find that  $R_r = 0.0645$ . Substituting this into (3.22) we can find  $M_r$  as a function of  $\gamma$  only. The value of the radial eigenvalue as a

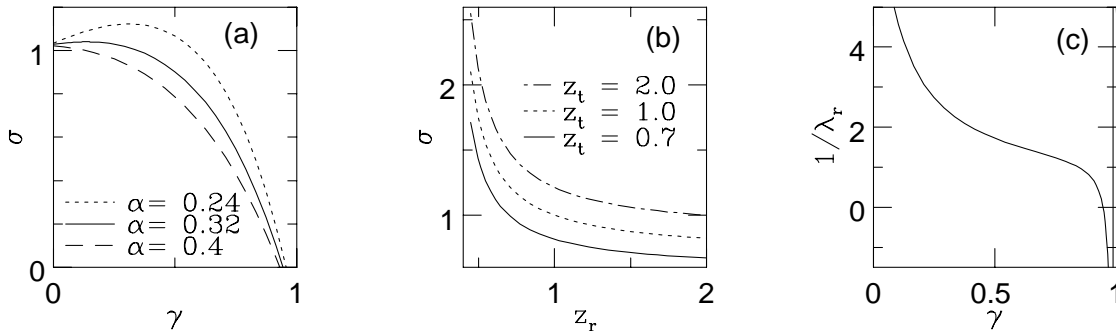


**Figure 4.** (a)  $\sigma$  versus  $\gamma$  for different values of  $\alpha$ . (b)  $\sigma$  versus radial source redshift  $z_r$  for various values of tangential source redshift  $z_t$ . (c) Radial magnification at the location of the tangential arc plotted versus  $\gamma$  for  $R_t = 0.2$  and  $R_r = 0.0645$ .

function of position is then given by

$$\lambda_r(R_r) = 1 - \frac{2M_r(\gamma)((1-\gamma)R_r^{-\gamma} - R_r^{2-2\gamma})}{(1 + R_r^{2-\gamma})^2}. \quad (3.25)$$

The radial magnification is just  $1/\lambda_r$ . In Fig. 4 (c), the radial magnification at the position of the tangential arc is plotted as a function of  $\gamma$ . In order to obtain a value of the magnification which is of order unity, we must choose  $\gamma$  in the range  $0.6 \lesssim \gamma \lesssim 0.95$ . Fig. 4 (a) shows that values of  $\gamma$  in the range  $0.6 \lesssim \gamma \lesssim 0.7$  correspond to acceptable values of  $\sigma$ . In other words, the problem pointed out by Bartelmann is assuaged by a choice of a cluster lens that is more singular than the dark halo profile of Navarro, Frenk & White (1996).

#### 4 THE ISOTHERMAL DOUBLE POWER-LAW MODEL

One of the double power-law models has a remarkable property – the lens equation can be re-cast as a solvable, quadratic equation for the image positions in terms of the source position. This is the model with an isothermal cusp. This property of invertibility is exceedingly scarce. It is possessed by only two other known models – the Schwarzschild lens (Einstein 1936; Refsdal 1964) and the infinite isothermal sphere (Kovner 1987a).

##### 4.1 The Image Positions

When  $\gamma = 1$ , the convergence diverges like  $R^{-1}$  at small radii and like  $R^{-3}$  at large radii, viz;

$$\kappa(R) = \frac{M}{R(1+R)^2}, \quad \psi = 2M \log(1+R). \quad (4.1)$$

Deprojecting the surface density by the well-known Abel inversion formula (e.g., Binney & Tremaine 1987), we find that the spherical cluster has three-dimensional density

$$\rho(r) = \begin{cases} \frac{\mathcal{M}}{2\pi^2} \left[ \frac{2r^2 + 1}{(1-r^2)^2 r^2} - \frac{3\text{arcosh}(1/r)}{(1-r^2)^{5/2}} \right], & r \leq 1, \\ \frac{\mathcal{M}}{2\pi^2} \left[ \frac{2r^2 + 1}{(r^2-1)^2 r^2} - \frac{3\text{arccos}(1/r)}{(r^2-1)^{5/2}} \right], & r \geq 1. \end{cases} \quad (4.2)$$

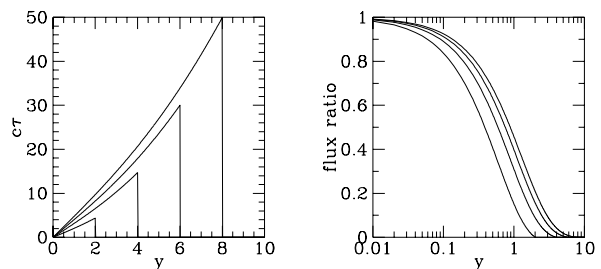


**Figure 5.** The variation of the time delay  $\tau$  and flux ratio of the images with separation of the source  $y$  from exact alignment with the isothermal double power-law lens. The curves are shown for total mass  $M = 1, 2, 3$  and  $4$  respectively. As  $y \rightarrow 2M$ , the second image becomes fainter and fainter. It finally disappears when the source crosses the pseudo-caustic at  $y = 2M$ . At this point, the notion of a time delay loses its meaning. (Units used with  $\xi_c^2 D_s(1+z_d)/(cD_d D_{ds}) = 1$ .)

Here,  $r$  is the three-dimensional radius in units of the length scale. A careful Taylor expansion shows the density is regular at  $r = 1$  and has the value:

$$\rho(1) = \frac{\mathcal{M}}{5\pi^2}. \quad (4.3)$$

The three-dimensional density diverges like  $r^{-2}$  at small radii and like  $r^{-4}$  at large radii. The model is therefore akin to the famous halo model of Jaffe (1983). We shall refer to it as *the isothermal double power-law model*. The deflection angle at a displacement  $x$  is

$$\Theta = \nabla\psi = \frac{2M \text{sign}(x)}{1 + |x|}. \quad (4.4)$$

The circle  $|y| = 2M$  is the pseudo-caustic. Source positions with  $|y| < 2M$  give two images whereas those with  $|y| > 2M$  give only one. The additional image is created or destroyed at the cusp. The pseudo-critical curves have degenerated into a point at the centre.

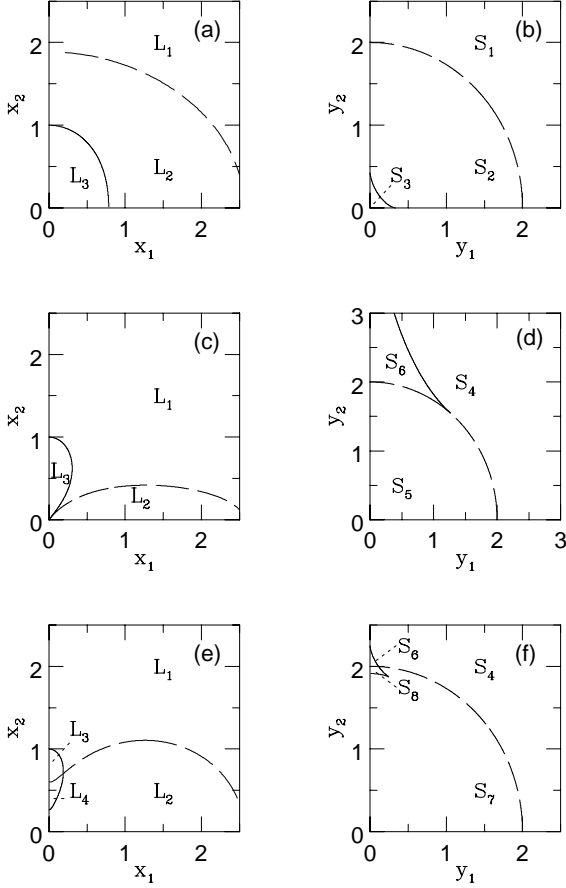


**Figure 6.** The critical curve and caustic topologies for the isothermal double power-law model perturbed with external shear. In each case, the lens plane is shown on the left, the source plane on the right. In panels (a) and (b),  $C_1 > C_2 > 0$  and there is one C point on each axis; (c) and (d),  $C_1 > 0, 0 > C_2 > -0.5$  and there is one C point on the  $x_2$ -axis and one S point at the origin; in (e) and (f)  $C_1 > 0, C_2 < -0.5$  and there is a C point and an F point on the  $x_2$ -axis. The caustics and critical curves are drawn in full lines, the pseudo-caustics and pseudo-critical curves are drawn in broken lines. (Units used with  $M = 1$ .)

Taking  $y > 0$  without loss of generality, the images are located on either side of the source at

$$x = \frac{1}{2}(y \mp 1) \pm \frac{1}{2}A_{\pm}(y), \quad (4.5)$$

with

$$A_{\pm}(y) = \sqrt{(y \pm 1)^2 + 8M}, \quad (4.6)$$

provided the source lies within the pseudo-caustic. The image at  $x > 0$  is of type I, the image at  $x < 0$  is of type II. If the source lies outside the pseudo-caustic, then only the former image is present. When  $|y| > 2M$ , the total magnification is

$$\mu = \frac{1}{2} + \frac{1}{2y} \frac{y(y+1) + 4M}{A_+(y)}, \quad (4.7)$$

**Table 2.** Image Positions as a Function of Source Positions as Labelled on Figs 6 and 7. Roman numerals are used to indicate the quadrant in which the image lies.

$S_1$	$L_{1I}$
$S_2$	$L_{2I}, L_{3III}$
$S_3$	$L_{2I}, L_{2II}, L_{3II}, L_{3III}$
$S_4$	$L_{1IV}$
$S_5$	$L_{2III}, L_{2IV}$
$S_6$	$L_{1III}, L_{1IV}, L_{3III}$
$S_7$	$L_{2IV}, L_{2III}$
$S_8$	$2L_{2III}, L_{2IV}, L_{4III}$
$S_9$	$L_{1III}$
$S_{10}$	$L_{2III}, L_{3III}$

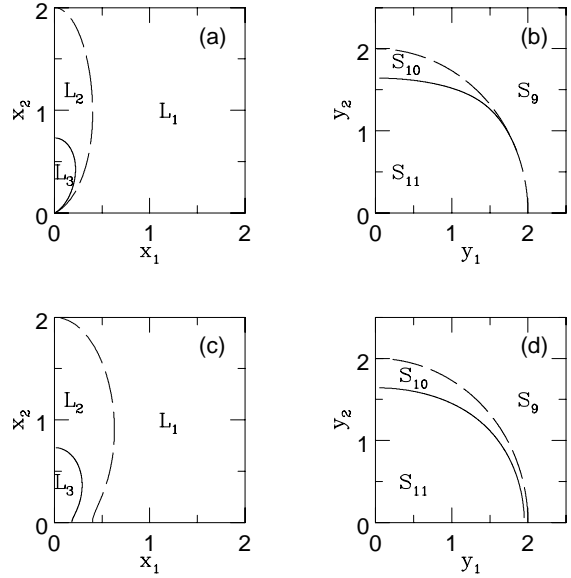


**Figure 7.** The critical curve and caustic topologies for the isothermal double power-law model perturbed with external shear (continued). In panels (a) and (b),  $0 > C_1 > -0.5 > C_2$  and there is an F point on the  $x_2$ -axis and an S point at the origin; in (c) and (d),  $-0.5 > C_1 > C_2$  and there is one F point on each axis. The caustics and critical curves are drawn in full lines, the pseudo-caustics and pseudo-critical curves are drawn in broken lines. (Units used with  $M = 1$ .)

whereas when  $|y| < 2M$ , it is

$$\mu = \frac{1}{2y} \left[ \frac{y(y+1) + 4M}{A_+(y)} + \frac{y(y-1) + 4M}{A_-(y)} \right]. \quad (4.8)$$

The time delay  $\tau$  is also explicit. For any source position

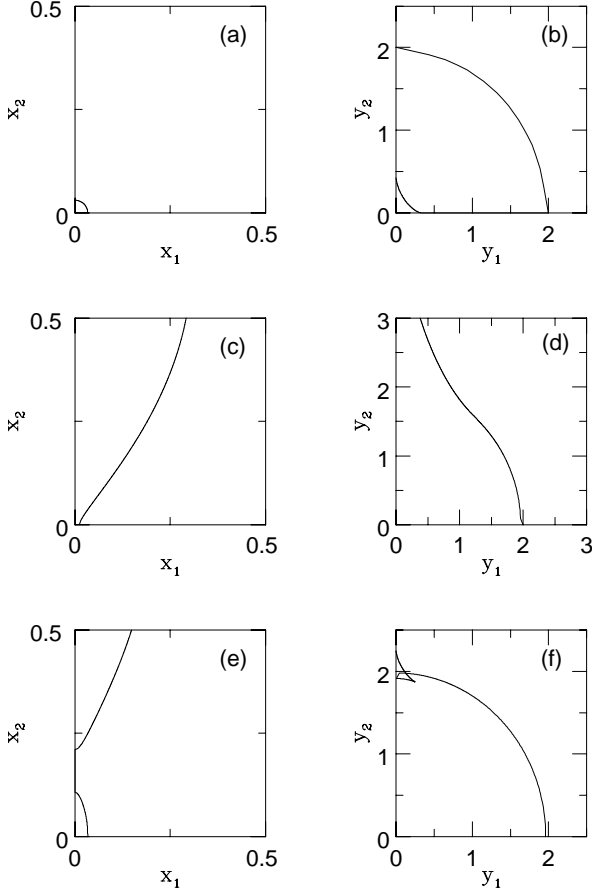


**Figure 8.** As Fig. 6 but for an isothermal double power-law model with true core. This causes the replacement of the pseudo-caustics with true caustics and the destruction of the pseudo-critical curves. In each case, the central portion of the lens plane is shown on the left, the source plane on the right. In panels (a) and (b),  $C_1 > C_2 > 0$  and there is one C and one F point on each axis. Only the tiny inner radial critical curve is visible in the plot. The outer tangential critical curve is virtually unchanged from Fig. 6. In panels (c) and (d),  $C_1 > 0, 0 > C_2 > -0.5$  and there is one C point on the  $x_2$ -axis and one F point on the  $x_1$ -axis. In panels (e) and (f),  $C_1 > 0, C_2 < -0.5$  and there is one F point on the  $x_1$  axis and a C point and two F points on the  $x_2$ -axis. (Units used with  $M = 1$ .)

which generates two images, it is

$$c\tau = \frac{\xi_c^2 D_s (1 + z_d)}{D_d D_{ds}} \left[ \frac{1}{4}(y+1)A_+(y) + \frac{1}{4}(y-1)A_-(y) - y + 2M \log \left| \frac{1+y+A_+(y)}{1-y+A_-(y)} \right| \right], \quad (4.9)$$

where  $z_d$  is the redshift of the lens. Fig. 5 shows the variation of the time delay and the flux ratio of the images with separation of the source  $y$  from exact alignment. For the images to be of comparable brightness, we require  $y \lesssim 1$ . The time delay is then approximately

$$c\tau \approx \frac{\sqrt{2M} \xi_c^2 D_s (1 + z_d)}{D_d D_{ds}}, \quad (4.10)$$

and so scales roughly like  $M^{1/2}$ .

## 4.2 Caustic Topology of the Perturbed Lens

The aim of this section is to classify the structure of the caustics and critical lines of the perturbed isothermal model exactly. This job has already been performed for the Plummer model (the instance  $\gamma = 0$  in (3.11)) in chapter 8 of Schneider, Ehlers & Falco (1992). The isothermal double power-law model has a pseudo-caustic not present in the Plummer model. The slightest breakage of the circular symmetry causes the pseudo-critical curves to be displaced from the density singularity. These unusual features mean that it is well-worth classifying the caustic topology for this model.

The lens action is considered as taking place in the presence of an external larger-scale gravitational field with local surface mass density  $\frac{1}{2}\Gamma_1 + \frac{1}{2}\Gamma_2$  and local shear  $\frac{1}{2}\Gamma_1 - \frac{1}{2}\Gamma_2$ . By choosing the orientation of the coordinates to diagonalise the tidal field, the lens equation becomes

$$\underline{y} = \underline{x} \left[ 1 - \frac{2M}{|\underline{x}|(1+|\underline{x}|)} \right] - \begin{pmatrix} \Gamma_1 & 0 \\ 0 & \Gamma_2 \end{pmatrix} \underline{x}. \quad (4.11)$$

Even in the presence of shear, the circle  $|y| = 2M$  remains as the pseudo-caustic. The pseudo-critical curves are now

$$\cos^2 \theta = \frac{4M(1+\Gamma_2) - r(1+\Gamma_2[\Gamma_2-2])}{(\Gamma_1-\Gamma_2)(r[\Gamma_1+\Gamma_2-2]-4M)}, \quad (4.12)$$

where  $(r, \theta)$  are polar coordinates in the lens plane.

Let us introduce the shorthand

$$C_1 = \frac{M}{1-\Gamma_1}, \quad C_2 = \frac{M}{1-\Gamma_2}. \quad (4.13)$$

Considering the first quadrant (i.e.,  $x_1 > 0, x_2 > 0$ ), critical points (C points) on the  $x_1$ -axis occur at

$$x_1 = \frac{1}{2}(1+8C_2)^{\frac{1}{2}} - \frac{1}{2}. \quad (4.14)$$

These exist provided  $C_2 > 0$ . Folds (F points) occur at

$$x_1 = \sqrt{-2C_1} - 1, \quad (4.15)$$

provided  $C_1 < -\frac{1}{2}$ . Alternatively, the fold can occur at the density singularity itself, when we refer to it as an S point. The discussion for the  $x_2$ -axis is similar with trivial changes of indices.

Figures 6 and 7 show the topologies of both the lens  $(x_1, x_2)$  and source  $(y_1, y_2)$  planes for the distinct image configurations. In Figs 6 (a) and (b), there is one C point on each axis. In Table 2, the image regions corresponding to the different regions of the source plane are listed. For example, a source in region  $S_3$  produces four images, one in  $L_2$  in the first quadrant ( $L_2I$ ), one in  $L_2$  in the second quadrant ( $L_2II$ ) and two in  $L_3$  in the second and third quadrants ( $L_3II, L_3III$ ). Moving the source from  $S_3$  to  $S_2$  causes the two images in the second quadrant to fuse and only two images are left, one in the first quadrant ( $L_2I$ ) and one in the third ( $L_3III$ ). If the source is now moved across the pseudo-caustic from  $S_2$  to  $S_1$ , the image in the third quadrant vanishes into the central density singularity, while the image in the first quadrant ( $L_1I$ ) remains. As expected, when the source crosses the pseudo-caustic, the number of images changes by one. Regions  $L_1, L_2$  and  $L_3$  correspond to images of types I, I and II respectively. There is no change in parity on crossing the pseudo-caustic. In Figs 6 (c) and (d), there is a C

point on the  $x_2$ -axis and an S point at the origin. Whenever a critical curve ends at an S point, the corresponding caustic is discontinuous. As is evident in the diagram, the caustic terminates abruptly in the source plane as it touches the pseudo-caustic. Sources in  $S_6$  generate three images (see Table 2). One image is lost on crossing the pseudo-caustic from  $S_6$  to  $S_5$ , whereas one image is gained on crossing the pseudo-caustic from  $S_4$  to  $S_5$ . Regions  $L_1$ ,  $L_2$  and  $L_3$  correspond to images of types II, II and III respectively. In Figs 6 (e) and (f), there is both a C point and an F point on the  $x_2$ -axis. Sources in  $S_8$  have four images (see Table 2). Traversing the pseudo-caustic from  $S_6$  to  $S_8$  or from  $S_4$  to  $S_7$  causes the gain of a single image. Regions  $L_1, L_2, L_3$  and  $L_4$  correspond to images of types II, II, III and III respectively. If  $0 > C_1 > C_2 > -0.5$  there are no critical points on the axes. Sources with  $|y| > 2M$  possess one image, source with  $|y| < 2M$  possess no images. The pseudo-critical curve lies at the origin.

The remaining two possible topologies are shown in Fig. 7. They are included for completeness, but are not physical, as there are regions of the source plane that correspond to no images in the lens plane. At first sight, this seems to contravene the theorem of Schneider (1984). If the time delay increases quadratically far from the lens, it seems that there must be at least one minimum of the Fermat surface. The reason why this theorem no longer holds here is that the values of the shear  $\Gamma_1$  and  $\Gamma_2$  now exceed unity. The Fermat potential decreases quadratically far from the lens and so there must be a highest point on the Fermat surface – but this corresponds to the density spike and not an image. A somewhat similar occurrence takes place in the singular point mass with shear or Chang-Refsdal lens (see Schneider, Ehlers & Falco, 1992, p. 261). In Figs 7 (a) and (b), there is an F point on the  $x_1$ -axis and an S point at the origin. Figs 7 (c) and (d) show a similar configuration, but with an F point on each axis. In both cases, sources in  $S_9$  give rise to one image of type III in region  $L_1$ . Crossing the pseudo-caustic from  $S_9$  to  $S_{10}$  generates a second image of type II in  $L_3$ , while the pre-existing image moves from  $L_1$  to  $L_2$ . However, as the source crosses the caustic to  $S_{11}$ , both images merge and disappear into the central density singularity. Note that in Fig. 7 (b), the crossing of the pseudo-caustic from  $S_9$  to  $S_{11}$  is accompanied by the destruction of a single image whereas the crossing from  $S_9$  to  $S_{10}$  is accompanied by the creation of a single image. Sources in  $S_{11}$  have no images at all.

As an aid to understanding, it is helpful to introduce a tiny core into the isothermal double power-law model so that it becomes

$$\kappa = \frac{M}{(R + \epsilon)(1 + R)^2}, \quad (4.16)$$

with corresponding deflection angle

$$\Theta = \frac{2M \text{sign}(x)}{(1 - \epsilon)(1 + |x|)} - \frac{2M\epsilon}{|x|(1 - \epsilon)^2} \log \left[ \frac{|x| + \epsilon}{\epsilon(1 + |x|)} \right]. \quad (4.17)$$

The changes in the topology of the caustics and the critical curves are shown in detail in Fig 8. This figure is directly comparable with the cases examined in Fig 6. The introduction of the infinitesimal core causes the conversion of the pseudo-caustics into true caustics, as is evident on comparing Figs 8 (b) and (f) with Figs 6 (b) and (f). Now, the

number of images changes by two on crossing these curves. The pseudo-critical curves are completely destroyed by the introduction of the core. Replacing them are tiny critical curves generated near the origin. For example, Figs 8 (a) and (e) show the emergence of a minute radial critical curve from the origin because of the infinitesimal core. Only the inner portion of the lens plane is shown in the figures – the outer critical curve is virtually unchanged from the singular model in Figs 6 and 7. So, not all the critical points on axis are visible in the details of the central regions. In Fig. 8 (d), only part of the pseudo-caustic is converted to a caustic, the remaining part being destroyed. In the lens plane, the S point of Fig. 6 (c) becomes an F point in Fig. 8 (c).

## 5 THE POWER-LAW LENSES

In this section, we study density cusps of infinite extent with elliptic equipotentials. Lenses with equipotentials stratified on similar concentric ellipses have been studied before (e.g., Kovner 1987b; Blandford & Kochanek 1987; Kochanek & Blandford 1987; Kassiola & Kovner 1993; Witt 1996; Witt & Mao 1997), although the emphasis has generally been on models with softened cores. By contrast, our interest is focused on the lenses with central density singularities.

### 5.1 The Potential-Convergence Pair

The deflection potential is

$$\psi = A[x_1^2 + x_2^2 q^{-2}]^{1-\gamma/2}, \quad (5.1)$$

where  $q$  is the axis ratio of the equipotentials,  $\gamma$  is the cusp index and the constant  $A$  fixes the overall scaling. All the models have infinite total projected mass.

As Contopoulos (1954) noted, three-dimensional distributions that are stratified on similar concentric ellipsoids project to two-dimensional distributions stratified on similar concentric ellipses. The projected potential (5.1) therefore corresponds to the three-dimensional galaxy models written down by Evans (1993, 1994) and called the power-law galaxies. Schneider, Ehlers & Falco (1992) caution that models with elliptical equipotentials may not be very realistic, so it is worth pointing out that the power-law galaxies have been successfully used to represent the nearby elliptical M32 (van der Marel et al. 1994) as well as the inner 500 parsecs of the Galactic bulge (Evans & de Zeeuw 1994). The convergence is cusped like

$$\kappa = \frac{A(2 - \gamma)}{2q^2} \frac{ax_1^2 + bx_2^2}{(x_1^2 + x_2^2 q^{-2})^{1+\gamma/2}}, \quad (5.2)$$

with

$$a = 1 - q^2(1 - \gamma), \quad b = 1 - q^{-2}(1 - \gamma). \quad (5.3)$$

The axis ratio of the equipotentials  $q$  describes the flattening of the model and can be restricted to lie in the range  $0 \leq q \leq 1$  without loss of generality. The projected mass density of the singular models has ellipticity  $\epsilon$

$$\epsilon = 1 - q \left[ \frac{q^2 - \gamma + 1}{1 + q^2(1 - \gamma)} \right]^{1/\gamma}. \quad (5.4)$$

The convergence is positive if  $\gamma < 1 + q^2$  (e.g., Blandford & Kochanek 1987). If the model is viewed as a projected

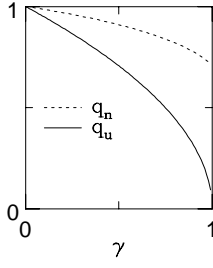


**Figure 9.** The critical values of  $q$  for naked cusps ( $q_n$ ) and the umbilic catastrophe ( $q_u$ ) plotted as functions of  $\gamma$

power-law galaxy, the constraints that the three-dimensional density and that the two-integral distribution function are positive definite are more severe and given in Evans (1994). The parameter  $\gamma$  describes the rotation curve of the model. If  $\gamma = 1$ , the model has an asymptotically flat rotation curve (e.g., Binney & Tremaine 1987; Evans 1993). If  $\gamma > 1$ , the rotation curve is declining, whereas if  $\gamma < 1$ , the rotation curve is rising. The range of  $\gamma$  is normally restricted to  $0 < \gamma < 2$ . The lower limit comes from requiring the convergence to vanish at spatial infinity, the upper limit is the Keplerian case of a point mass.

The tangential critical curve has intercepts

$$x_{1,t}^2 = \left[ Aq^{-2}(2-\gamma) \right]^{2/\gamma}, \quad (5.5)$$

$$x_{2,t}^2 = q^2 \left[ A(2-\gamma) \right]^{2/\gamma}. \quad (5.6)$$

The condition for the existence of a tangential critical curve is

$$A(2-\gamma) > 0. \quad (5.7)$$

It is always satisfied. If the cusp is strong ( $\gamma > 1$ ), there is a transition from two to four images on crossing the tangential caustic. If the cusp is weak ( $\gamma < 1$ ), there is a transition from one to three images. The radial critical curve has intercepts

$$x_{1,r}^2 = \left[ A(2-\gamma)(1-\gamma) \right]^{2/\gamma}. \quad (5.8)$$

$$x_{2,r}^2 = q^2 \left[ Aq^{-2}(2-\gamma)(1-\gamma) \right]^{2/\gamma}. \quad (5.9)$$

The radial critical curve exists only if  $\gamma < 1$ . Quintuple imaging occurs if

$$A(2-\gamma)(1-\gamma) > 0. \quad (5.10)$$

That is, quintuple imaging can occur for all power-law galaxies with weak cusps. The critical curves become smaller both in the limit of increasing homogeneity ( $\gamma \rightarrow 0$ ) and in the Keplerian point mass limit ( $\gamma \rightarrow 2$ ).

In the source plane, the semi-axes of the tangential and radial caustics are

$$\frac{y_{2,t}}{y_{1,t}} = \frac{y_{1,r}}{y_{2,r}} = q^{2/\gamma-1}. \quad (5.11)$$

For  $\gamma < 1$ , there are two important topology changes that can occur. For models only weakly perturbed from circular

symmetry, the radial caustic lies entirely outside the tangential caustic. Models flatter than the critical flattening  $q_n$  given by

$$q_n^2 = 1 - q_n^{2/\gamma} \gamma (1-\gamma)^{1/\gamma-1}, \quad (5.12)$$

possess “naked cusps”. That is, two of the cusps of the tangential caustic lie outside the radial caustic. The umbilic catastrophe occurs at a critical flattening  $q_u$  given by

$$q_u^2 = 1 - \gamma. \quad (5.13)$$

Fig. 9 shows the behaviour of the critical axis ratio  $q_n$  and  $q_u$  for the onset of naked cusps and the umbilic catastrophe respectively as a function of cusp index  $\gamma$ .

For the moment, let us consider the model without external shear. In general, the lens equation must be solved numerically. However, when the source is on-axis and aligned with the lens, the image positions and magnifications can be found exactly. This is sufficiently uncommon for non-axisymmetric lenses that it is worth giving the solution explicitly. There are always two images on the minor axis at  $(0, \pm x_2)$ , where

$$x_2 = q \left[ \frac{A(2-\gamma)}{q^2} \right]^{1/\gamma}. \quad (5.14)$$

These have even parity and the magnification  $\mu$  is

$$\mu = \frac{1}{\gamma(1-q^2)}. \quad (5.15)$$

There are always two images on the major axis at  $(\pm x_1, 0)$ , where

$$x_1 = \left[ A(2-\gamma) \right]^{1/\gamma}. \quad (5.16)$$

These have odd parity and the magnification  $\mu$  is

$$\mu = \frac{q^2}{\gamma(1-q^2)}. \quad (5.17)$$

Only these four images occur when the cusp is strong. For weak cusps, there is an additional (infinitely de-magnified) image of even parity at the origin. The total magnification  $A_{\text{tot}}$  is

$$A_{\text{tot}} = \frac{2(1+q^2)}{\gamma(1-q^2)}. \quad (5.18)$$

This equation is exact when the source is on-axis and is approximate when the source lies within the tangential caustic. This equation has previously been given by Kassiola & Kovner (1993) for the special case  $\gamma = 1$ .

The  $\gamma = 1$  model has the characteristic properties of an isothermal cusp. Unlike the perturbed circular model of Section 4.2, it has a truly non-axisymmetric pseudo-caustic. Its equation can be calculated by the methods of Section 2.2. If the phase of  $z = x_1 + ix_2$  is  $\theta$  and the phase of  $z_s = y_1 + iy_2$  is  $\phi$ , then the equation of the pseudo-caustic is

$$\begin{aligned} |z_s|^2 = y_1^2 + y_2^2 &= \left( \frac{\partial \psi}{\partial x_1} \right)^2 + \left( \frac{\partial \psi}{\partial x_2} \right)^2 \\ &= \frac{A^2(\cos^2 \theta + q^{-4} \sin^2 \theta)}{\cos^2 \theta + q^{-2} \sin^2 \theta}. \end{aligned} \quad (5.19)$$

As the source crosses the pseudo-caustic, an extra image of type II is generated at the density singularity. On the

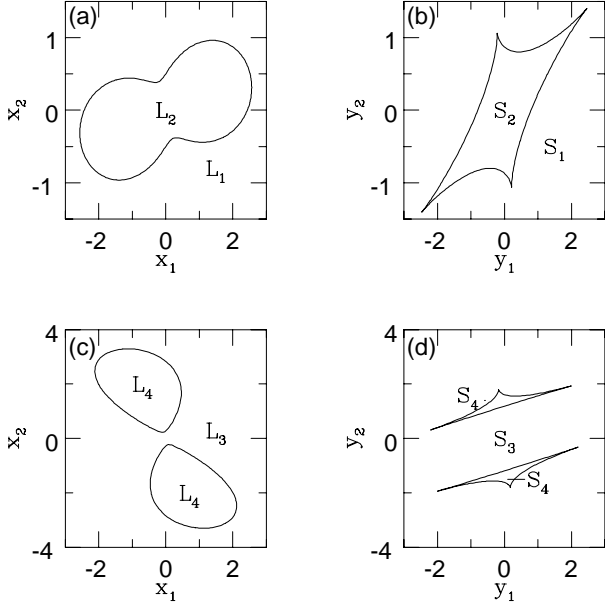


**Figure 10.** The critical curve and caustic topologies for the power-law lenses in the presence of external shear. In each case, the lens plane is shown on the left, the source plane on the right. This figure is for the case of a strong cusp with  $\gamma = 1.25$  and  $q = 0.6$ . [Figs 10 (a) and (b) have  $\Gamma_1 = 0.1, \Gamma_2 = 0.5$ , Figs 10 (c) and (d) have  $\Gamma_1 = 0.8, \Gamma_2 = 0.7$ ]

pseudo-caustic, we know from the lens equation that the relation between the two phases is

$$\tan \theta = q^{-2} \tan \phi, \quad (5.20)$$

and so the pseudo-caustic is an ellipse of form

$$y_1^2 + q^2 y_2^2 = A^2. \quad (5.21)$$

The pseudo-caustic is concentric with the elliptic equipotentials, but it is elongated in the opposite direction. For this model, the lens equation can be reduced to a quartic equation. The quartic degenerates to simpler quadratics if the source lies either on the major axis or on the minor axis. Suppose the source lies on the major axis at  $(y_1, 0)$ , with  $y_1 > 0$  without loss of generality. Then there is one image if  $y_1 > A$  at

$$x_1 = y_1 + A, \quad x_2 = 0. \quad (5.22)$$

Initially, this image has even parity. Its magnification is

$$\mu = \frac{A + y_1}{|y_1 - A(q^{-2} - 1)|}. \quad (5.23)$$

On crossing the pseudo-caustic at  $y_1 = A$ , there is a second image generated at

$$x_1 = y_1 - A, \quad x_2 = 0. \quad (5.24)$$

It has odd parity and finite magnification

$$\mu = \frac{A - y_1}{A(q^{-2} - 1) + y_1}. \quad (5.25)$$

On crossing the tangential caustic at  $y_1 = A(q^{-2} - 1)$ , the image (5.22) changes from even to odd parity. Simultane-

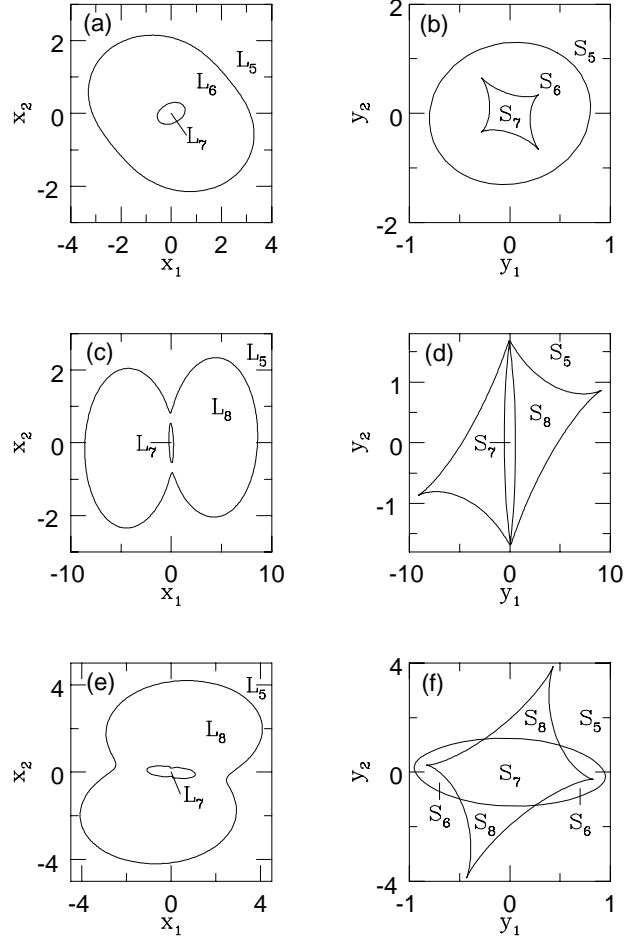


**Figure 11.** As in Figure 10, but for the case of a weakly cusped power-law lens with  $\gamma = 0.75$  and  $q = 0.6$ . [Figs 11 (a) and (b) have  $\Gamma_1 = -0.5, \Gamma_2 = -0.1$ , Figs 11 (c) and (d) have  $\Gamma_1 = 0.3, \Gamma_2 = 0.1$  and Figs 11 (e) and (f) have  $\Gamma_1 = -0.7, \Gamma_2 = 0.1$ ]

ously, two new images of even parity are generated at

$$x_1 = \frac{y_1}{(1 - q^2)}, \quad x_2 = \pm \frac{1}{q} \left[ A^2 - \frac{y_1^2}{(q^{-2} - 1)^2} \right]^{1/2}. \quad (5.26)$$

The magnification of each image is

$$\mu = \frac{A^2 q^{-2} (q^{-2} - 1)}{A^2 (q^{-2} - 1)^2 - y_1^2}. \quad (5.27)$$

Note that a change in parity of one of the pre-existing images must occur on crossing a pseudo-caustic for our general theorems of Section 2.2 to hold good. The images and magnifications when the source lies on the minor axis can be found similarly.

## 5.2 Caustic Topology of the Perturbed Lens

Figures 10 and 11 show the possible topologies of the caustics for the power-law lenses in the presence of external shear. In this case, the lens equations become

$$y_1 = x_1 \left[ 1 + \Gamma_1 - \frac{A(2 - \gamma)}{(x_1^2 + x_2^2 q^{-2})^{\gamma/2}} \right] + \Gamma_2 x_2, \quad (5.28)$$

**Table 3.** Image Positions as Function of Source Positions as Labelled on Figs 10 and 11.

S <sub>1</sub>	L <sub>1</sub> , L <sub>2</sub>
S <sub>2</sub>	2L <sub>1</sub> , 2L <sub>2</sub>
S <sub>3</sub>	2L <sub>3</sub>
S <sub>4</sub>	3L <sub>3</sub> , L <sub>4</sub>
S <sub>5</sub>	L <sub>5</sub>
S <sub>6</sub>	L <sub>5</sub> , L <sub>6</sub> , L <sub>7</sub>
S <sub>7</sub>	2L <sub>5</sub> , 2L <sub>6</sub> , L <sub>7</sub>
S <sub>8</sub>	2L <sub>5</sub> , L <sub>8</sub>

and

$$y_2 = x_2 \left[ 1 - \Gamma_1 - \frac{Aq^{-2}(2-\gamma)}{(x_1^2 + x_2^2 q^{-2})^{\gamma/2}} \right] + \Gamma_2 x_1, \quad (5.29)$$

where the shear matrix is taken as traceless and of form:

$$\Gamma = \begin{pmatrix} \Gamma_1 & \Gamma_2 \\ \Gamma_2 & -\Gamma_1 \end{pmatrix}. \quad (5.30)$$

These equations have been recently considered by Witt & Mao (1997), who prove a number of interesting theorems regarding the image positions. Since the shear axes do not, in general, coincide with the major and minor axes of the lens potential, the symmetry axes of the caustics are also different from those of the lens. Consequently, Table 3 – which gives the image regions corresponding to different regions in the source plane – does not contain information about which quadrants will contain the images. The quadrant in which a given image is found varies according to the exact position of the source.

Fig. 10 shows the two distinct topologies which occur for a strong cusp ( $\gamma = 1.25$ ). When the external shear is small compared to the lens shear, there is only one critical curve in the lens plane and a corresponding caustic in the source plane, as shown in Figs 10 (a) and (b). A source in region S<sub>2</sub> produces four images, two in region L<sub>1</sub> of the lens plane and two in region L<sub>2</sub>. Moving the source from S<sub>2</sub> to S<sub>1</sub> causes two of these images to fuse together leaving only two images, one in region L<sub>1</sub> and the other in region L<sub>2</sub>. If  $\Gamma_1$  and  $\Gamma_2$  satisfy

$$\Gamma_1^2 + \Gamma_2^2 = 1, \quad (5.31)$$

then the caustic becomes extremely elongated along the axis

$$y_2 = \frac{\Gamma_2}{1 + \Gamma_1}. \quad (5.32)$$

The result of further increasing the shear so that  $\Gamma_1^2 + \Gamma_2^2 > 1$  is shown in Figs 10 (c) and (d) – there are now two critical curves and two caustics. A source in region S<sub>4</sub> produces four images, three in region L<sub>3</sub> and one in region L<sub>4</sub>. If the source is moved from S<sub>4</sub> to S<sub>3</sub>, two of the images fuse and only two images are left, both lying in region L<sub>3</sub>. It is also possible to have a situation in which there is no caustic.

Fig. 11 shows the three possible critical curve and caustic topologies for the case of a weak cusp ( $\gamma = 0.75$ ). Figs 11

(a) and (b) show the radial caustic lying entirely outside the tangential caustic. Alternatively, as in Figs 11 (c) and (d), the tangential critical curve can completely contain the radial caustic. For intermediate values of the shear, the tangential curve can lie partly outside the radial curve and partly inside, as shown in Figs 11 (e) and (f). If we continue to increase the magnitude of the external shear, the outer curve in Fig. 11 (d) is observed to be stretched along its major axis while being simultaneously compressed along its minor axis. When  $\Gamma_1$  and  $\Gamma_2$  satisfy (5.31), this curve becomes a straight line. Outside the unit circle in the  $(\Gamma_1, \Gamma_2)$  plane, there exists only one caustic, with two cusps.

In Figs. 11 (a) and (b), a source placed in region S<sub>7</sub> produces five images as expected for a weak cusp. There are two in region L<sub>5</sub>, two in L<sub>6</sub> and one in L<sub>7</sub>. If the source is moved across the caustic to region S<sub>6</sub>, one pair of images fuses together to leave three images, one in each of the regions L<sub>5</sub>, L<sub>6</sub> and L<sub>7</sub>. Finally, if the source is moved to region S<sub>5</sub> another pair of images fuses to leave a single image in region L<sub>5</sub>. The locations of the images corresponding to the source regions in Figs. 11 (d) and (f) can be found from Table 3. As described above, if  $\Gamma_1$  and  $\Gamma_2$  lie outside the unit circle in the  $(\Gamma_1, \Gamma_2)$  plane, the tangential critical curve no longer exists. Sources placed inside the one remaining caustic give three images (two lie outside the critical curve and one lies inside) while those placed outside give only one image lying outside the critical curve.

## 6 CONCLUSIONS

This paper has studied the properties of lenses with central density cusps. These are models in which the convergence  $\kappa$  diverges as a function of projected radius  $R$  like

$$\kappa \propto R^{-\gamma}, \quad (6.1)$$

near the centre. Numerical simulations (e.g., Navarro, Frenk & White 1996), dynamical arguments (e.g., Evans & Collett 1997) and observations (e.g., Lauer et al. 1995; Faber et al. 1997) all suggest that galaxies and clusters commonly have such singular density profiles. By generalising the index theorem to allow for central density singularities, we suggest the following classification of cusps on the basis of their lensing properties:

(1) Strong density cusps ( $1 < \gamma < 2$ ) give rise to an even number of images. There are as many images of odd parity as there are images of even parity ( $n_I - n_{II} + n_{III} = 0$ ). Models with strong cusps do not possess radial caustics.

(2) Weak density cusps ( $0 < \gamma < 1$ ) give rise to an odd number of images. The images of even parity outnumber the images of odd parity by one ( $n_I - n_{II} + n_{III} = 1$ ). Models with weak cusps possess radial caustics. Even though such models are singular, they can produce radial arcs (cf. Mellier, Fort & Kneib 1993; Bartelmann 1996).

(3) Isothermal density cusps ( $\gamma = 1$ ) always possess *pseudo-caustics*. If the source is within the pseudo-caustic, there is an even number of images ( $n_I - n_{II} + n_{III} = 0$ ). If the source is outside the pseudo-caustic, there is an odd number ( $n_I - n_{II} + n_{III} = 1$ ). A method for computing the location of the pseudo-caustic is given. Note that the pseudo-caustic differs from a true caustic in two ways. First, the

magnification of a point source is finite, not infinite, at the pseudo-caustic. Second, the number of images created or destroyed on crossing the pseudo-caustic is one, not two. A circular lens, even if perturbed by external shear, has a pseudo-caustic that is a circle. This is not the case if the lens is truly non-axisymmetric.

As specific examples, we have presented two families of models. The double power-law family has a central cusp, a transition region and an outer envelope. The power-law family are a set of elliptical cusps of infinite extent. They are projected power-law galaxies. In both cases, detailed properties of the individual lenses are given, together with a classification of the caustic structures in the presence of external shear. As an application, we consider a problem pointed out by Bartelmann (1996). He suggested that lensing may be problematic for the cusped Navarro, Frenk & White (1996) density profile in cases where both radial and tangential arcs are present. On matching the positions of the arcs, this model predicts large values for the radial magnification at the tangential arc, which in turn implies that the corresponding sources must be radially very thin. We have shown that this problem is not so serious for lenses that have more singular density cusps – and, indeed, higher resolution simulations of halo formation suggest that the cusp slope may have been originally underestimated (Fukushige & Makino 1997; Moore et al 1997).

Our investigation has uncovered a new model – *the isothermal double power-law model* – for which the lens equation is exactly solvable for any source position. This scarce property is only possessed by two other known circularly symmetric lenses, the Schwarzschild lens and the isothermal sphere. The isothermal double power-law model has a three-dimensional density which behaves like  $r^{-2}$  in the centre and like  $r^{-4}$  in the outer parts, so it is a realistic model for a galaxy or cluster of finite extent with a flat rotation curve. As the image positions are explicitly available, the lensing cross-sections are straightforward to calculate.

## ACKNOWLEDGMENTS

NWE thanks the Royal Society for financial support. MW acknowledges financial support from a Scatcherd Scholarship. The paper was partly written at the Aspen Center for Physics. We particularly wish to thank Chris Kochanek, Donald Lynden-Bell and Prasenjit Saha for a number of helpful conversations.

## REFERENCES

- Abramowitz M., Stegun I., 1965, Handbook of Mathematical Functions, Dover, New York, chap. 26
- Bahcall J. N., Wolf R. A., 1976, ApJ, 209, 214
- Bartelmann M., 1996, AA, 313, 697
- Binney J.J., Tremaine S.D., 1987, Galactic Dynamics, Princeton University Press, Princeton, chap. 2
- Blandford R., Kochanek C., 1987, ApJ, 321, 658
- Blandford R., Narayan R., 1986, ApJ, 310, 568
- Burke W. L., 1981, ApJ, 244, L1
- Contopoulos G., 1954, Z. Astrophys., 35, 67
- Einstein A., 1936, Science, 84, 506
- Evans N. W., 1993, MNRAS, 260, 191
- Evans N. W., 1994, MNRAS, 267, 333
- Evans N. W., Collett J. L., 1997, ApJ, 480, L103
- Evans N. W., de Zeeuw P. T., 1994, MNRAS, 271, 202
- Faber et al., 1997, ApJ, in press (astro-ph/9610055)
- Fort B., Le Fèvre O., Hammer F., Cailloux M., 1992, ApJ, 339, L125
- Fukushige T., Makino J., 1997, ApJ, 477, L9
- Fukuyama T., Okamura T., ApJ, submitted (astro-ph/9702061)
- Gebhardt K. et al., 1996, AJ, 112, 105
- Gradshteyn I. S., Ryzhik I. M., 1980, Tables of Integrals, Series and Products, Academic Press, San Diego
- Hernquist L., 1990, ApJ, 356, 359
- Jaffe W., 1983, MNRAS, 202, 995
- Kassiola A., Kovner I., 1993, ApJ, 417, 450
- Keeton C. R., Kochanek C., ApJ, 1997, submitted (astro-ph/9705194)
- Kochanek C., 1996, ApJ, 473, 595
- Kochanek C., Blandford R., 1987, ApJ, 321, 676
- Kormann P., Schneider P., Bartelmann M., 1994, AA, 284, 285
- Kovner I., 1987a, ApJ, 312, 22
- Kovner I., 1987b, Nat, 325, 507
- Lauer T. R., et al. 1995, AJ, 110, 2622
- MacKenzie R. H., 1985, JMP, 26, 1592
- Mellier Y., Fort B., Kneib J.-P., 1993, ApJ, 407, 33
- Moore B., Governato F., Quinn T., Stadel J., Lake G., 1997, ApJ, submitted (astro-ph/9709051)
- Navarro J., Frenk C. S., White S. D. M. 1996, ApJ, 462, 563
- Ramsey A. S., 1940, An Introduction to the Theory of Newtonian Attraction, Cambridge University Press, Cambridge, chap 3
- Refsdal S., 1964, MNRAS, 128, 307
- Routh E. J., 1892, A Treatise on Analytical Statics, volume 2, Cambridge University Press, Cambridge, p. 25
- Schneider P., 1984, AA, 140, 119
- Schneider P., Ehlers J., Falco E., 1992, Gravitational Lensing, Springer, New York.
- van der Marel R. P., Evans N. W., Rix H. W., White S. D. M., & de Zeeuw P. T., 1994, MNRAS, 271, 99
- Witt H., 1990, AA, 236, 311
- Witt H., 1996, ApJ, 472, L1
- Witt H., Mao S., 1997, MNRAS, submitted (astro-ph/9702021)
- Zhao H. S., 1997, MNRAS, 278, 488

This paper has been produced using the Royal Astronomical Society/Blackwell Science  $\text{\TeX}$  macros.